

Article

The Organic Bromide Sources Adjusting the Shape and Band Structures of BiOBr Nanosheets for Enhanced Photodegradation Performances of BPA

Donghao Xia, Kaiyang Sun, Youwei Zeng, Lulu Wang, Yi Zhang, Jie Shen *, Zhaohui Wu * and Wenhui Feng *

Hunan Key Laboratory of Applied Environmental Photocatalysis, Changsha University, Changsha 410022, China; xdh910672740@163.com (D.X.); s19163323744@163.com (K.S.); zyw210970@163.com (Y.Z.); wll_13928@163.com (L.W.); zhangyi2000521@163.com (Y.Z.)

* Correspondence: calfensj@gmail.com (J.S.); hubeiwzh1624@126.com (Z.W.); fengwenhui1991@126.com (W.F.); Tel.: +86-731-84261421 (J.S.)

Abstract: Bismuth oxybromide (BiOBr) nanosheets were prepared by employing organic bromide sources. In the presence of organic bromide sources, the effects of different conditions on the band structure, shape, size, and light responses of BiOBr nanosheets were examined. The reaction conditions, including different types of organic bromide sources, solvent, concentration, temperature, and time, were examined regarding the formation of BiOBr nanosheets. Then, the photocatalytic performances of different BiOBr nanosheets were also examined. Especially, the BiOBr nanosheets obtained from the addition of over 2 mmol of tetramethyl ammonium bromide (TMAB) in mannitol or EG at a higher temperature and longer reaction time showed superior photocatalytic activity. The enhanced photocatalytic performance of bisphenol A over these BiOBr nanosheets was achieved within 50 min due to efficient charge transfer and separation.

Keywords: organic bromide sources; shape; BiOBr nanosheets; photocatalytic performances



Citation: Xia, D.; Sun, K.; Zeng, Y.; Wang, L.; Zhang, Y.; Shen, J.; Wu, Z.; Feng, W. The Organic Bromide Sources Adjusting the Shape and Band Structures of BiOBr Nanosheets for Enhanced Photodegradation Performances of BPA. *Catalysts* **2022**, *12*, 820. <https://doi.org/10.3390/catal12080820>

Academic Editors: Amr Fouda and Mohammed F. Hamza

Received: 13 May 2022

Accepted: 28 June 2022

Published: 26 July 2022

Publisher's Note: MDPI stays neutral with regard to jurisdictional claims in published maps and institutional affiliations.



Copyright: © 2022 by the authors. Licensee MDPI, Basel, Switzerland. This article is an open access article distributed under the terms and conditions of the Creative Commons Attribution (CC BY) license (<https://creativecommons.org/licenses/by/4.0/>).

1. Introduction

Bismuth oxybromide (BiOBr), with a unique lamellar sandwich structure consisting of double halide and $[\text{Bi}_2\text{O}_2]^{2+}$ layers, has received considerable attention in the photocatalysis of contaminant removal, nitrogen fixation, and CO_2 reduction [1–5]. Many routes have been used to prepare BiOBr nanosheets with different surface properties, sizes, and band structures [2,3,6–9], providing distinctive photocatalytic performances. During the synthesis process, inorganic bromide salts, including potassium bromide (KBr) [10,11], sodium bromide (NaBr) [12], and organic bromide compounds containing cetyltrimethylammonium bromide (CTAB) [7,13,14], are frequently used as the bromide sources for BiOBr. Comparatively, the organic cationic ions of CTAB not only act as bromide sources but also play a role of a template, resulting in much thinner BiOBr nanosheets and enhanced photocatalytic activity [14]. Hence, the selection of CTAB is appealing for BiOBr preparation. For instance, a BiOBr lamellar structure was prepared with the assistance of CTAB using the hydrothermal route. Additionally, lamellar-structured BiOBr obtained at a fixed molar ratio of CTAB and $\text{Bi}(\text{NO}_3)_3$ and 160 °C for the whole day exhibited a superior photocatalytic efficiency under visible-light irradiation. Compared with BiOBr obtained by KBr, the resulting photocatalytic performances of these BiOBr nanosheets were about four times [14]. Recently, other organic bromides with different cationic groups, such as 1-butyl-3-methylimidazolium bromide [3] and ionic liquid of $[\text{C}_{16}\text{mim}]\text{Br}$ [15], have also been employed for the preparation of the atomic layer or ultra-thin BiOBr nanosheets, in the presence of or without exfoliation assistance. For instance, 1-butyl-3-methylimidazolium bromide was employed to synthesize BiOBr nanosheets via the hydrothermal route, which were exfoliated easily to obtain BiOBr nanosheets with an atomic thickness and oxygen

vacancies. Then, the resulting BiOBr ultrathin nanosheets could achieve a CO generation rate of $87.4 \text{ mmol g}^{-1} \text{ h}^{-1}$ by converting CO_2 , which was 24 times higher than that of unexfoliated bulk BiOBr nanosheets [3]. However, whether the types of organic cationic groups have significant effects on the shape, size, surface, and band structure of BiOBr nanosheets is still unknown. Herein, we selected small molecular organic bromide with different lengths and different cationic groups for the preparation of BiOBr nanosheets. Then, the variation in the shape, size, band structure, and photocatalytic performances of the BiOBr nanosheets was examined, aiming to exploit the crucial factors to control the preparation of the BiOBr nanosheets.

2. Results and Discussion

2.1. Effects of Organic Bromide Sources, Solvent, and Concentration on the Shape and Phase Control of BiOBr Nanosheets

Firstly, the products were prepared by altering the inorganic and organic bromide sources in aqueous solution. The XRD patterns of the resulting different products are shown in Figure 1a. Obviously, all the samples were indexed to the tetragonal BiOBr (JCPDS No. 09-0393) (Figure 1a). Enlarging the partial XRD patterns in the range of $31.0\text{--}33.5^\circ$, the samples obtained by the addition of KBr, TBAB, and CTAB were well-matched with BiOBr. However, the sample obtained by the addition of TMAB slightly shifted to lower 2θ , indicating that the crystal lattices were slightly expanded probably due to the intercalation of the small molecules of TMAB (Figure 1b) [16,17]. All the resulting BiOBr exhibited a predominant light response within the range of $200\text{--}450 \text{ nm}$ (Figure 1c). Additionally, the corresponding estimated band gaps of BiOBr were $\sim 2.77 \text{ eV}$. Furthermore, regardless of the bromide sources, BiOBr showed an irregular sheet-like morphology in the aqueous solution (Figure 1d–g).

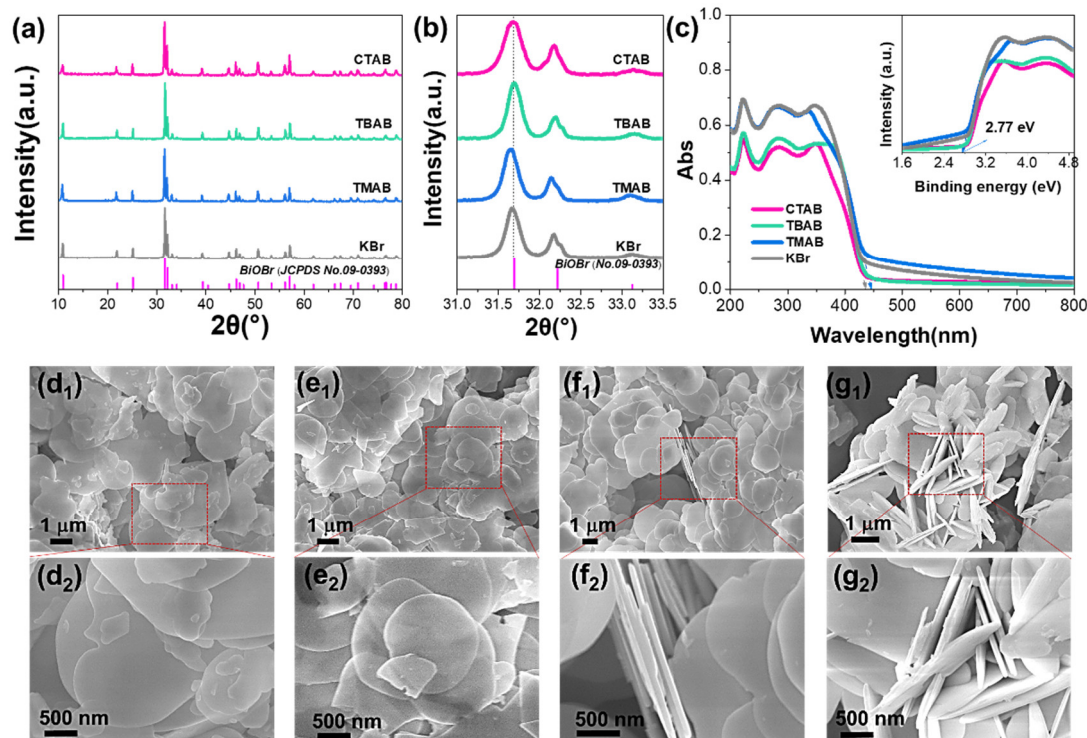


Figure 1. Comparison of products obtained by altering the bromide ion sources, (a) XRD patterns; (b) corresponding enlarged range of $31\text{--}33.5^\circ$. (c) DRS spectra (inset with corresponding estimated bandgaps). SEM images of (d₁) and (d₂) KBr, (e₁) and (e₂) TMAB, (f₁) and (f₂) TBAB, and (g₁) and (g₂) CTAB.

The phases, light response, and morphologies of the resulting samples showed significant differences according to the solvents (Figure 2). The XRD patterns of the products obtained in H₂O and 0.02 M of mannitol solution were similar, which were well-indexed to BiOBr (JCPDS No. 09-0393) (Figure 2a). Additionally, the intensity of the characteristic peak located at 31.7° (corresponding to (102) planes) was higher than that at 32.2° (corresponding to the (110) planes). However, the intensity of these characteristic peaks was reversed by employing EG as the solvent. Furthermore, these peaks located at 25.1° (corresponding to the (101) planes), 31.7°, and 32.2° were broadened and the intensity of all peaks decreased, indicating the decreasing crystallinity of the resulting BiOBr. These peaks broadened continuously, the (102) planes vanished, and the crystallinity of the products also decreased when G was selected as the solvent (Figure 2b,c). Then, the resulting XRD patterns were more likely to be Bi₄O₅Br₂ (ICSD No. 94498) [18,19]. When the solvent was changed from H₂O to G, the viscosity was gradually increased. Apparently, the increasing viscosity of the acholic solvents retarded the mass transfer for nucleation and growth [20,21], and hindered the crystallinity of the resulting products, and even changed its phase.

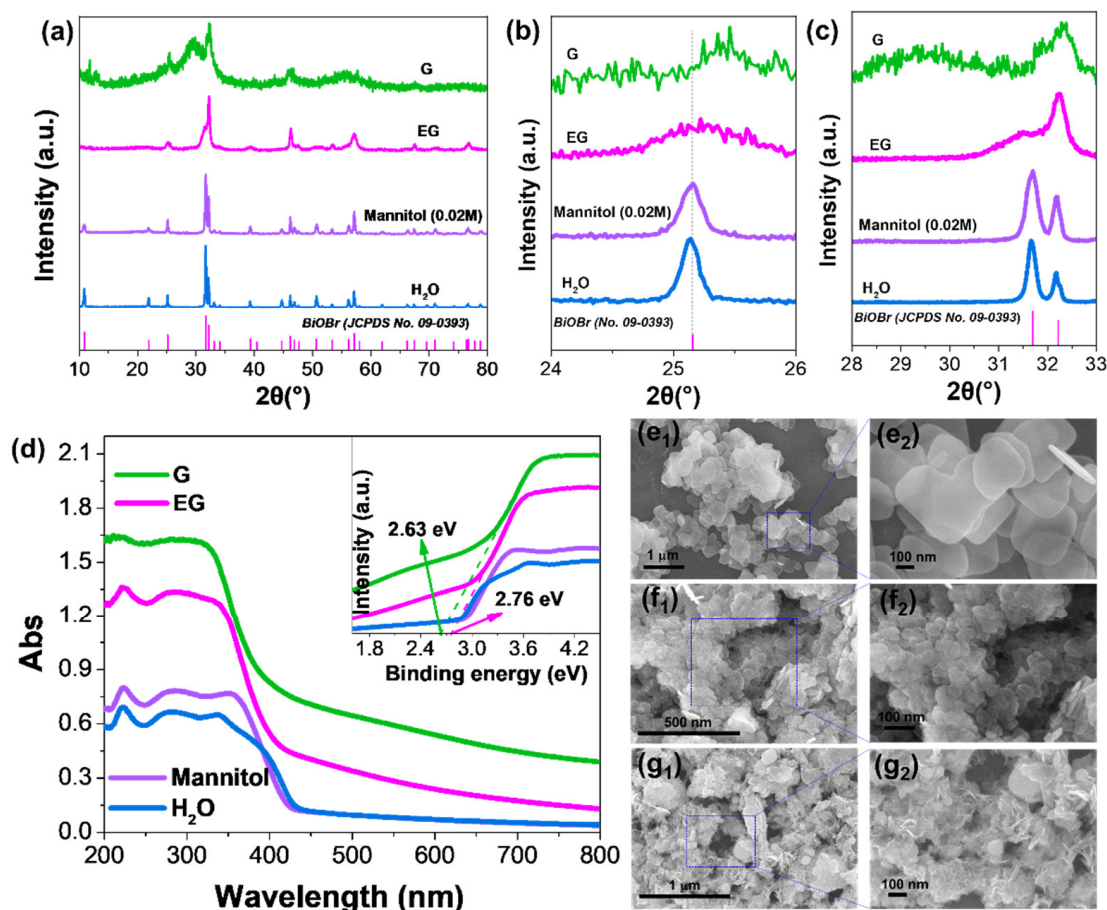


Figure 2. Comparison of different products prepared in different solvents, (a) XRD patterns, corresponding enlarged range of (b) 24–26° and (c) 28–33°. (d) DRS spectra (inset with corresponding estimated bandgaps). SEM images of (e₁) and (e₂) mannitol (0.02 M), (f₁) and (f₂) EG, and (g₁) and (g₂) G.

The light response of BiOBr obtained from mannitol solution was similar to that obtained in water. However, for BiOBr obtained from solvents of EG and G, the light absorption band edges broadened, and there was also an obvious absorption tail covering the visible region (Figure 2d). The estimated band gaps of the resulting BiOBr gradually narrowed down after changing the solvent from H₂O to G (Figure 2d). All prepared

samples showed a sheet-like morphology; however, the size of the resulting sheets was gradually decreased by altering the solvent from H₂O to EG. Specifically, the average size of the BiOBr nanosheets obtained from EG was ~50 nm, which was much smaller than that obtained from H₂O and mannitol (~400 nm), whereas the assembled BiOBr flowers were obtained from G (Figure 2e–g).

When the concentration of the reactants in the mannitol solution was increased from 1 to 4 mmol, the XRD patterns of all the samples were identical, which were all indexed to the tetragonal BiOBr (JCPDS No. 09-0393) (Figure 3a). Additionally, all the characteristic peaks were well-matched without shifting (Figure 3b,c). However, for BiOBr obtained at a lower concentration of reactant (1 mmol), the crystallinity decreased and some characteristic peaks were broader, indicating the generation of defects [12]. From the DRS spectra, the light responses of the resulting products were also identical to each other, and only BiOBr obtained at a lower concentration of reactant (1 mmol) showed a slight band tail due to the defects. Correspondingly, the estimated band gaps of the resulting BiOBr decreased from 2.97 to 2.59 eV when the concentration of the reactants was decreased from 4 to 1 mmol (Figure 3d). Obviously, the decreasing concentration of TMAB could produce BiOBr nanosheets with a narrowed band gap. Furthermore, the shape of BiOBr obtained from the 1 mmol reactants showed an irregular edge sheet-like morphology but with an average size of ~1 μ m. When the concentration of TMAB was increased to over 2 mmol, the shape of BiOBr was maintained as a tetragonal sheet with a size of ~400 nm (Figures 2e and 3e,f). These results are consistent with the classical nucleation theory, where a higher concentration of reactant contributes to a massive number of nuclei but a smaller size due to higher supersaturation [20,21].

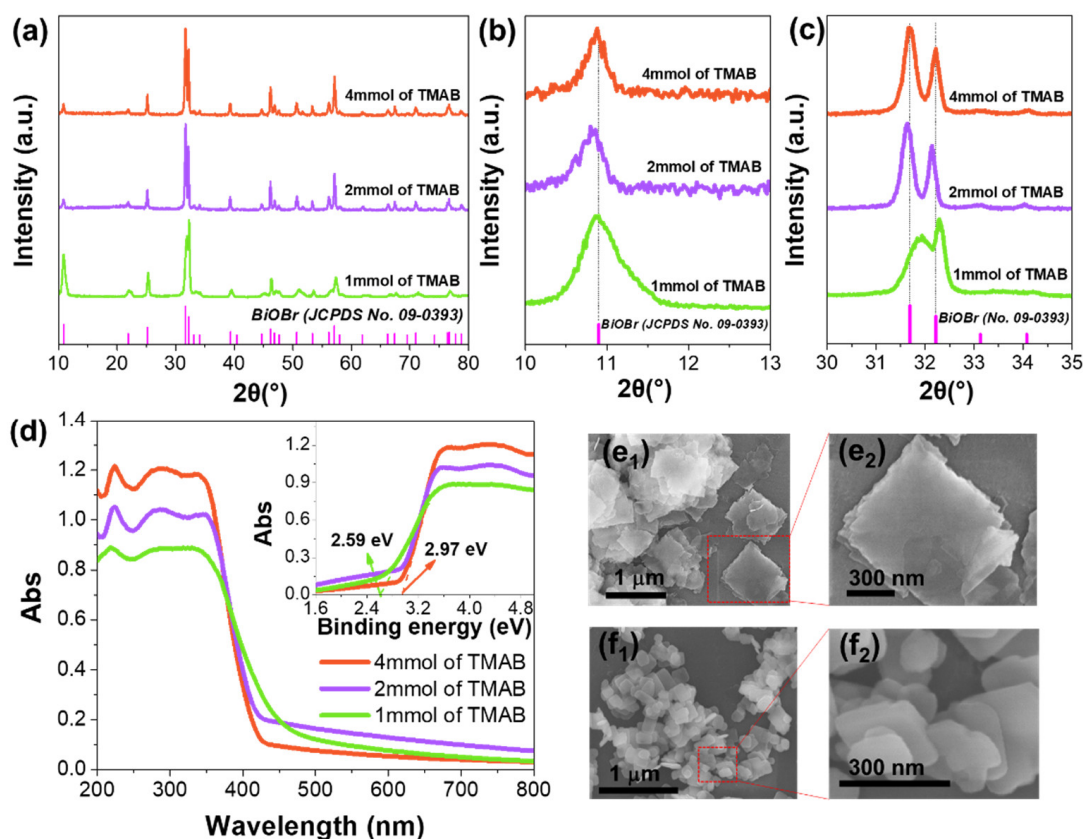


Figure 3. Comparison of products prepared by the addition of different molar reactants, (a) XRD patterns, corresponding enlarged range of (b) 10–13° and (c) 30–35°. (d) DRS spectra (inset with corresponding estimated bandgaps). SEM images of (e₁) and (e₂) 1 mmol of TMAB and (f₁) and (f₂) 4 mmol of TMAB.

When the reaction time was further prolonged from 2 to 12 h, and the reaction temperature increased from 120 to 180 °C, the resulting products were tetragonal BiOBr nanosheets in the presence of TMAB (Figure 4). Additionally, the light responses of these BiOBr nanosheets were barely altered (Figure 4b,d). Apparently, all the shapes of the resulting BiOBr were nanosheets in the mannitol solution (Figures 5 and S1), as proposed by the scheme shown in Figure 5a. However, when the reaction time and temperature were increased, the size of the resulting BiOBr nanosheets gradually increased due to Ostwald ripening (Figures 5 and S1) [22–24].

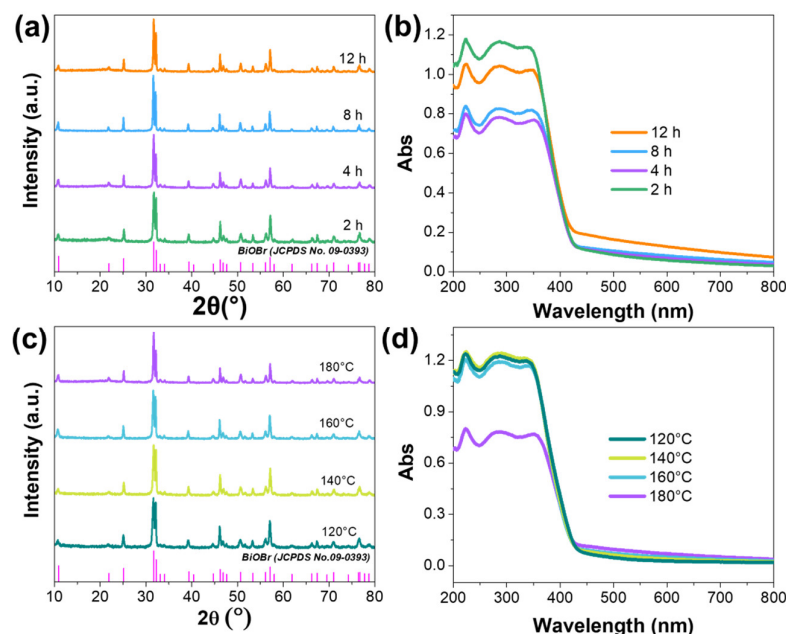


Figure 4. Comparison of products prepared in different times (a) XRD patterns, and (b) DRS spectra. Comparison of products prepared in different temperatures (c) XRD patterns, and (d) DRS spectra.

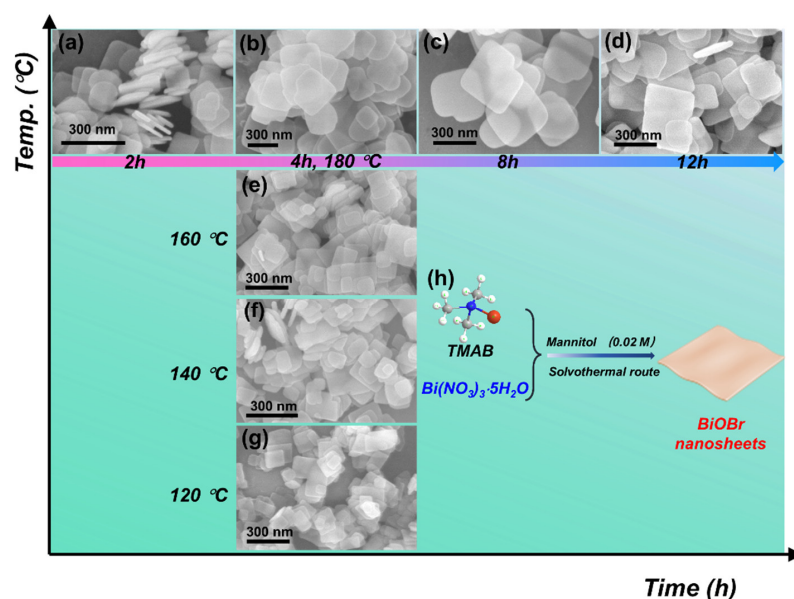


Figure 5. SEM images of the products obtained at different times when the reaction temperature was fixed at 180 °C: (a) 2 h, (b) 4 h, (c) 8 h, and (d) 12 h. SEM images of the products obtained at different temperatures when the reaction time was fixed at 4 h: (e) 160 °C, (f) 140 °C, and (g) 120 °C. (h) Schematic illustration of the synthetic process.

2.2. Structure Variations and Photocatalytic Performances of BiOBr Nanosheets

The sheet-like morphology of the resulting BiOBr obtained from the addition of 2 and 1 mmol of TMAB was confirmed by the TEM images (Figure 6a,d). In the high-resolution TEM (HRTEM) image of the BiOBr nanosheets obtained from the addition of 2 mmol of TMAB, clear and identical perpendicular crystal lattice fringes of 0.27 nm ascribed to the (110) atomic planes of BiOBr were observed. Further, lateral lattice spacing fringes of 0.81 nm ascribed to the (001) facets of BiOBr were also observed in the lateral HRTEM image. These results validated that BiOBr was predominately exposed to (001) facets. Similarly, the BiOBr nanosheets obtained from the addition of 1 mmol of TMAB also showed dominant (001) facet exposure (Figure 6e,f).

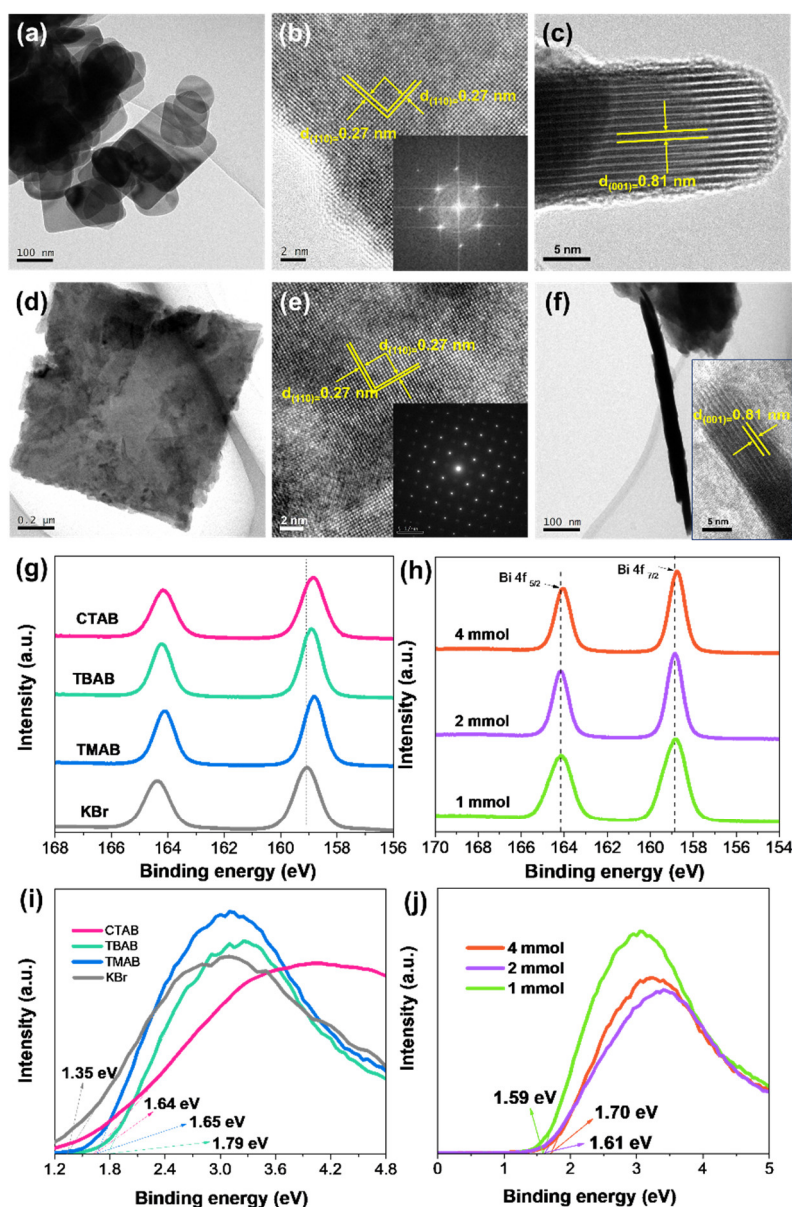


Figure 6. Comparison of different BiOBr, (a) TEM, (b) HRTEM (inset with FFT pattern), and (c) lateral HRTEM images of BiOBr prepared by the addition of 2 mmol of TMAB in mannitol. (d) TEM, (e) HRTEM (inset with SAED pattern), and (f) lateral TEM images of BiOBr prepared by the addition of 1 mmol of TMAB in mannitol (inset with the lateral HRTEM image of BiOBr). (g) Bi 4f and (h) Bi 4f XPS spectra comparisons of different products. Valence-band XPS of products obtained (i) from changing the bromide sources and (j) changing the concentration of the reactants.

In the Bi 4f spectra, the binding energy of Bi 4f_{7/2} and Bi 4f_{5/2} was 159.1 and 164.4 eV for the BiOBr nanosheets produced by the addition of KBr. Comparatively, the binding energy peaks of the BiOBr nanosheets prepared by the addition of TMAB and TBAB were shifted by ~0.2 eV to a lower binding energy, suggesting the organic bromide sources could redistribute more charges for BiOBr (Figure 6g) [25]. Furthermore, the unshifted binding energy of Bi 4f_{7/2} and Bi 4f_{5/2} of the BiOBr nanosheets obtained at different concentrations of the reactant sources also validated this point (Figure 6h). However, the band structures of these BiOBr nanosheets varied dramatically. For instance, the VB level of the BiOBr nanosheets obtained by the addition of KBr in aqueous solution was 1.35 eV while the VB levels of the BiOBr nanosheets obtained at TMAB, TBAB, and CTAB were shifted to a more positive level of 1.65, 1.79, and 1.57 eV, respectively. Additionally, for the BiOBr nanosheets prepared at increasing reactant concentrations, the VB levels were slightly shifted from 1.50 to 1.70 eV. When the band gaps of different BiOBr samples were combined, the corresponding conduction band (CB) levels of BiOBr prepared by the addition of KBr, TMAB, TBAB, and CTAB in H₂O were −1.47, −1.12, −1.05, and −1.18 eV, respectively. These CB levels were similar to the estimated Fermi energy levels according to the Mott–Schottky plots (Figure S2). Additionally, the CB levels of BiOBr obtained from increasing the reactant concentration from 1 to 4 mmol in mannitol solution were −1.00, −1.24, and −1.27 eV, respectively. Obviously, the band structure of BiOBr can be regulated by the bromide sources and the concentration of the reactants.

Under the full spectra, the photocatalytic performances of BPA over different BiOBr nanosheets were investigated. In Figure 7a, the BiOBr nanosheets prepared by the introduction of TMAB into aqueous solution exhibited superior photocatalytic performances, where an almost ~55% photocatalytic efficiency was obtained within 50 min, which is ~2 times more than that of other BiOBr nanosheets. Such enhanced photocatalytic performances of BPA over the BiOBr nanosheets (obtained at TMAB) are probably due to the intercalation of tetramethyl ammonium groups into the BiOBr structure. Then, the intercalated groups act as a bridge for charge transfer [26,27], rather than through the intrinsic internal electric field of BiOBr [28,29]. Additionally, the BiOBr nanosheets obtained from the reactant concentration of over 2 mmol exhibited higher photocatalytic performances due to the significantly reduced size and defects (Figure 7b). Additionally, BiOBr nanosheets prepared in EG, or obtained at higher temperatures and during longer times in mannitol solution showed higher photocatalytic activity owing to the dramatically reduced size of the BiOBr nanosheets and increased crystallinity, respectively (Figure S3). Furthermore, the photocatalytic performances of the BiOBr nanosheets produced in mannitol (or 2 mmol of reactants) were maintained even after three cycles, demonstrating its higher stability (Figure 7c).

During the photocatalytic process, the charge carriers' transfer and the separation efficiency of BiOBr were examined. The photocurrent signals of the BiOBr nanosheets prepared by the addition of TMAB in aqueous solution were higher than that of others, which is consistent with the photocatalytic performances, indicating the highest charge separation efficiency of this BiOBr nanosheet (Figure 7d). According to the EIS spectra, the BiOBr nanosheets prepared by the addition of TMAB in aqueous solution showed a smaller radius, implying a lower interfacial transfer resistance and faster separation of the charge carriers (Figure 7e). A plausible photocatalytic mechanism of the BiOBr nanosheets is proposed based on the results of the scavenger tests (Figure 7f and Figure S4). The proper band gap and band structure of BiOBr could promote efficient transfer and separation of charge carriers, where the separated electrons on the CB immigrate to the surface of BiOBr and react with the O₂ molecules of the solution ($O_2 + e^- \rightarrow \bullet O_2^-$) for $\bullet O_2^-$ [30], which act as the predominant active species for photocatalysis, similarly to previous reports [8,19,31].

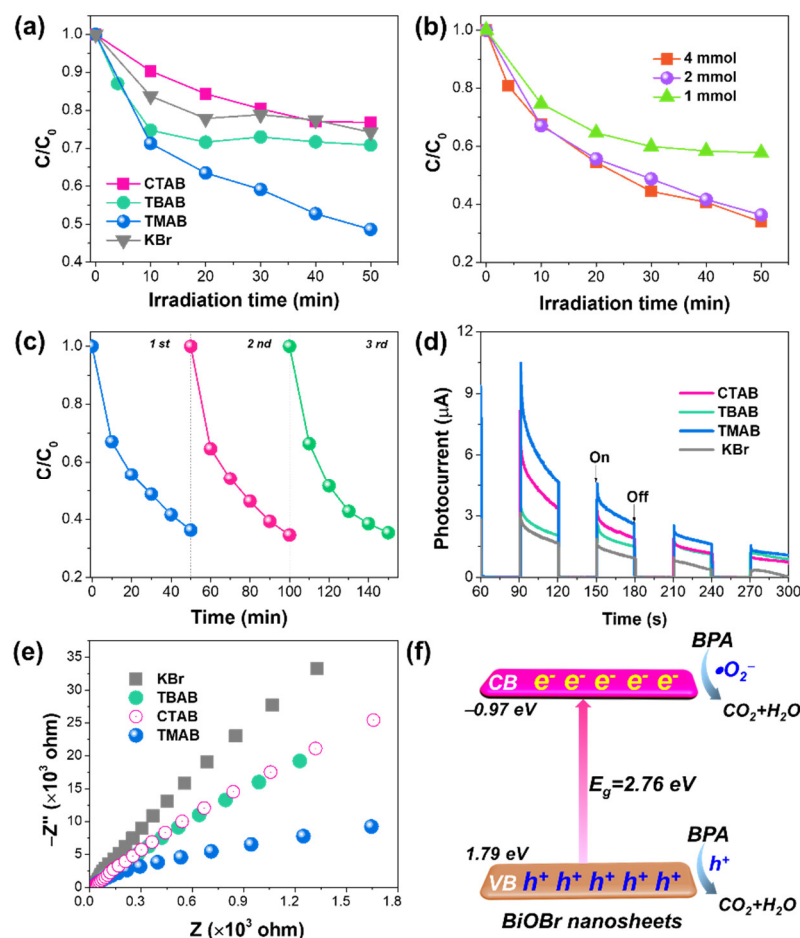


Figure 7. Photocatalytic performances of BPA over the obtained different products (a) by altering the bromide sources and (b) changing the concentration of the reactants. (c) Cycling photocatalytic performances of BiOBr nanosheets obtained in mannitol and in the presence of 2 mmol of TMAB. (d) Transient photocurrent density curves and (e) EIS spectra of different products. (f) Illustration of the photocatalytic process.

3. Experimental

3.1. Synthesis of BiOBr Nanosheets

All BiOBr nanosheets were synthesized via a solvothermal route. Typically, $\text{Bi}(\text{NO}_3)_3 \cdot 5\text{H}_2\text{O}$ was dissolved into solvents to form a homogenous solution or suspension, termed A. Simultaneously, 0.2 g of branched polyethyleneimine (BPEI) and different types and concentrations of bromide sources were dissolved in the same types of solvents as A to ultrasonically form a homogenous solution, termed B. Then, solution B was dropped into solution A slowly to form a white suspension, which was stirred for 30 min at room temperature. The resulting suspension was transferred to a Teflon-lined autoclave reactor for a certain time at a fixed temperature. During the reaction process, the bromide sources, including KBr, tetramethyl ammonium bromide (TMAB), tetrabutylammonium bromide (TBAB), and cetyltrimethylammonium bromide (CTAB), were selected. Additionally, the employed solvents were mannitol (0.2 mM), ethylene glycol (EG), glycerol (G), and mixed solvent of EG and G with a volume ratio of 1 to 1. The reaction temperature was changed from 120 to 180 °C, and the reaction time was altered from 2 to 12 h. All the reaction conditions are listed in Table S1. After the reaction, the reactor naturally cooled down, and the precipitation was washed and dried for further application.

3.2. Characterization

The shapes of the resulting products were recorded using transmission electron microscopy (TEM, Hitachi HT7700, Tokyo, Japan) and scanning electron microscopy (SEM, Hitachi SU-8010) images. The powder X-ray diffraction (XRD) patterns of all the resulting products were recorded on an X-ray diffractometer (SmartLab, Rigaku, Tokyo, Japan). X-ray photoelectron spectroscopy (XPS, Escalab 250 Xi, Thermo Fisher, Waltham, MA, USA) of some samples was performed. The light responses of the products were recorded on a UV-Vis spectrophotometer (UV-2600, Shimadzu, Kyoto, Japan) through the diffuse reflectance spectra (DRS). The photocurrent response and electrochemical impedance spectroscopy (EIS) of the resultants were recorded on an electrochemical workstation (CHI 660E, Beijing, China) using a three-electrode system in Na₂SO₄ solution (0.5 M).

3.3. Photocatalytic Activity

The photocatalytic performances of different samples were evaluated using photodegrading bisphenol A (BPA, 10 mg/L) solution under a Xenon lamp (Perfect light, PLS-SXE 300/300 UV, Beijing, China). Typically, photocatalysts (25 mg) were redispersed in 50 mL of BPA solution (10 mg/L). This suspension was maintained in darkness under stirring for 1 h to achieve equilibrium regarding adsorption-desorption. Then, the Xenon lamp was turned on and timing initiated. During the photocatalytic process, 2 mL of the reacted suspension was withdrawn intermittently. The solid photocatalysts were filtered using Millipore filters (0.22 µm), and the remaining transparent solution was analyzed on a UV-vis spectrophotometer (UVmini-1280, Shimadzu, Japan) to assess the concentration variation in BPA.

4. Conclusions

In summary, the effects of organic bromide sources on the band structure, shape, size, and phase of BiOBr nanosheets were thoroughly examined. Different organic bromide sources in different solvents with different reactant concentrations, times, and temperatures for BiOBr nanosheets with distinctive phases, light responses, and band structures were investigated. Then, the photocatalytic performances of the different BiOBr nanosheets were also examined. Especially, the BiOBr nanosheets obtained by the addition of over 2 mmol of TMAB in mannitol or EG and higher temperatures and longer reaction times showed superior photocatalytic activity due to the proper band structure for efficient charge transfer and separation.

Supplementary Materials: The following are available online at <https://www.mdpi.com/article/10.3390/catal12080820/s1>. Table S1. All the reactants and reaction conditions in this study; Figure S1. SEM images of samples prepared at different reaction time, (a) 2 h, (b) 4 h, (c) 8 h, (d) 12 h (inset with the corresponding average size of resulted samples); Figure S2. The Mott–Schottky plots of different samples electrodes at frequencies of 1000 Hz, versus the Ag/AgCl electrode; Figure S3. Photocatalytic performances of BiOBr nanosheets obtained at different conditions, (a) by adding different solvents, (b) at different reaction time, and (c) at different reaction temperature; Figure S4. Scavenger tests of BiOBr nanosheets obtained in mannitol and in the presence of 2 mmol of TMAB, 180 °C, 4 h. [32,33].

Author Contributions: Methodology, investigation, D.X., K.S. and Y.Z. (Youwei Zeng); data curation, writing—original draft, L.W. and Y.Z. (Yi Zhang); writing—review and editing, Z.W.; editing and polishing, J.S. and W.F. All authors have read and agreed to the published version of the manuscript.

Funding: This research was funded by the Scientific Research Fund of Hunan Provincial Education Department (20B055), and National Natural Science Foundation of China (52174238).

Data Availability Statement: This study did not report any data.

Conflicts of Interest: The authors declare no conflict of interest.

References

1. Yu, H.J.; Huang, H.W.; Xu, K.; Hao, W.C.; Guo, Y.X.; Wang, S.B.; Shen, X.L.; Pan, S.F.; Zhang, Y.H. Liquid-phase exfoliation into monolayered BiOBr nanosheets for photocatalytic oxidation and reduction. *ACS Sustain. Chem. Eng.* **2017**, *5*, 10499–10508. [\[CrossRef\]](#)
2. Ye, L.Q.; Jin, X.L.; Liu, C.; Ding, C.H.; Xie, H.Q.; Chu, K.H.; Wong, P.K. Thickness-ultrathin and bismuth-rich strategies for BiOBr to enhance photoreduction of CO₂ into solar fuels. *Appl. Catal. B-Environ.* **2016**, *187*, 281–290. [\[CrossRef\]](#)
3. Wu, J.; Li, X.D.; Shi, W.; Ling, P.Q.; Sun, Y.F.; Jiao, X.C.; Gao, S.; Liang, L.; Xu, J.Q.; Yan, W.S.; et al. Efficient visible-light-driven CO₂ reduction mediated by defect-engineered BiOBr atomic layers. *Angew. Chem. Int. Edit.* **2018**, *57*, 8719–8723. [\[CrossRef\]](#)
4. Wu, D.; Ye, L.Q.; Yip, H.Y.; Wong, P.K. Organic-free synthesis of {001} facet dominated BiOBr nanosheets for selective photoreduction of CO₂ to CO. *Catal. Sci. Technol.* **2017**, *7*, 265–271. [\[CrossRef\]](#)
5. Feng, H.F.; Xu, Z.F.; Wang, L.; Yu, Y.X.; Mitchell, D.; Cui, D.; Xu, X.; Shi, J.; Sannomiya, T.; Du, Y.; et al. Modulation of photocatalytic properties by strain in 2D BiOBr nanosheets. *ACS Appl. Mater. Inter.* **2015**, *7*, 27592–27596. [\[CrossRef\]](#)
6. Bhachu, D.S.; Moniz, S.J.A.; Sathasivam, S.; Scanlon, D.O.; Walsh, A.; Bawaked, S.M.; Mokhtar, M.; Obaid, A.Y.; Parkin, I.P.; Tang, J.W.; et al. Bismuth oxyhalides: Synthesis, structure and photoelectrochemical activity. *Chem. Sci.* **2016**, *7*, 4832–4841. [\[CrossRef\]](#) [\[PubMed\]](#)
7. Zhang, L.; Cao, X.F.; Chen, X.T.; Xue, Z.L. BiOBr hierarchical microspheres: Microwave-assisted solvothermal synthesis, strong adsorption and excellent photocatalytic properties. *J. Colloid. Interf. Sci.* **2011**, *354*, 630–636. [\[CrossRef\]](#)
8. Zhang, D.; Li, J.; Wang, Q.G.; Wu, Q.S. High {001} facets dominated BiOBr lamellas: Facile hydrolysis preparation and selective visible-light photocatalytic activity. *J. Mater. Chem. A* **2013**, *1*, 8622–8629. [\[CrossRef\]](#)
9. Wang, Z.D.; Chu, Z.; Dong, C.W.; Wang, Z.; Yao, S.Y.; Gao, H.; Liu, Z.Y.; Liu, Y.; Yang, B.; Zhang, H. Ultrathin BiOX (X = Cl, Br, I) nanosheets with exposed {001} facets for photocatalysis. *ACS Appl. Nano Mater.* **2020**, *3*, 1981–1991. [\[CrossRef\]](#)
10. Wang, H.; Yong, D.Y.; Chen, S.C.; Jiang, S.L.; Zhang, X.D.; Shao, W.; Zhang, Q.; Yan, W.S.; Pan, B.C.; Xie, Y. Oxygen-vacancy-mediated exciton dissociation in BiOBr for boosting charge-carrier-involved molecular oxygen activation. *J. Am. Chem. Soc.* **2018**, *140*, 1760–1766. [\[CrossRef\]](#)
11. Kong, X.Y.; Lee, W.P.C.; Ong, W.J.; Chai, S.P.; Mohamed, A.R. Oxygen-deficient BiOBr as a highly stable photocatalyst for efficient CO₂ reduction into renewable carbon-neutral fuels. *ChemCatChem.* **2016**, *8*, 3074–3081. [\[CrossRef\]](#)
12. Xue, X.L.; Chen, R.P.; Chen, H.W.; Hu, Y.; Ding, Q.Q.; Liu, Z.T.; Ma, L.B.; Zhu, G.Y.; Zhang, W.J.; Yu, Q.; et al. Oxygen vacancy engineering promoted photocatalytic ammonia synthesis on ultrathin two-dimensional bismuth oxybromide nanosheets. *Nano Lett.* **2018**, *18*, 7372–7377. [\[CrossRef\]](#) [\[PubMed\]](#)
13. Ye, Z.H.; Xiao, X.Y.; Chen, J.Y.; Wang, Y. Fabrication of BiVO₄/BiOBr composite with enhanced photocatalytic activity by a CTAB-assisted polyol method. *J. Photoch. Photobiol. A* **2019**, *368*, 153–161. [\[CrossRef\]](#)
14. Meng Shang, W.W. Ling Zhang, Preparation of BiOBr lamellar structure with high photocatalytic activity by CTAB as Br source and template. *J. Hazard. Mater.* **2009**, *167*, 803–809. [\[CrossRef\]](#)
15. Xia, J.X.; Ge, Y.P.; Di, J.; Xu, L.; Yin, S.; Chen, Z.G.; Liu, P.J.; Li, H.M. Ionic liquid-assisted strategy for bismuth-rich bismuth oxybromides nanosheets with superior visible light-driven photocatalytic removal of bisphenol-A. *J. Colloid. Interf. Sci.* **2016**, *473*, 112–119. [\[CrossRef\]](#) [\[PubMed\]](#)
16. Yun, J.N.; Zhang, Z.Y.; Yan, J.F.; Zhang, F.C. Effect of In-doping on electronic structure and optical properties of Sr₂TiO₄. *Chin. Phys. Lett.* **2009**, *26*, 067102.
17. Xing, Y.L.; Wang, J.X.; Chen, L.; Wang, A.Q.; Li, F.; Wang, C.; Zhong, E.Q. Synthesis and characterization of Cu-BiVO₄/MCM-41 composite catalysts with enhanced visible light photocatalytic activities. *J. Mater. Sci. Mater. El.* **2016**, *27*, 8633–8640. [\[CrossRef\]](#)
18. Wu, Z.; Wu, M.; Li, Z.; Pan, Y.; Qiu, J.; Li, T.; Xu, K.; Zhang, S.; Xu, D.; Guo, M. Regulating the phase transition of monoclinic Bi₄O₅Br₂ through the synergistic effect of “drag force” and facet recognition by branched polyethyleneimine. *Cryst. Eng. Comm.* **2020**, *22*, 5871–5881. [\[CrossRef\]](#)
19. Wu, Z.H.; Shen, J.; Ma, N.; Li, Z.F.; Wu, M.; Xu, D.F.; Zhang, S.Y.; Feng, W.H.; Zhu, Y.F. Bi₄O₅Br₂ nanosheets with vertical aligned facets for efficient visible-light-driven photodegradation of BPA. *Appl. Catal. B-Environ.* **2021**, *286*, 119937. [\[CrossRef\]](#)
20. Wu, Z.H.; Seok, S.; Kim, D.H.; Kim, W.S. Control of Crystal Size Distribution using Non-Isothermal Taylor Vortex Flow. *Cryst. Growth Des.* **2015**, *15*, 5675–5684. [\[CrossRef\]](#)
21. Liao, C.X.; Ma, Z.J.; Chen, X.F.; He, X.; Qiu, J.R. Controlled synthesis of bismuth oxyiodide toward optimization of photocatalytic performance. *Appl. Surf. Sci.* **2016**, *387*, 1247–1256. [\[CrossRef\]](#)
22. Zhang, C.W.; Xia, Y.; Zhang, Z.M.; Huang, Z.; Lian, L.Y.; Miao, X.S.; Zhang, D.L.; Beard, M.C.; Zhang, J.B. Combination of cation exchange and quantized Ostwald ripening for controlling size distribution of lead chalcogenide quantum dots. *Chem. Mater.* **2017**, *29*, 3615–3622. [\[CrossRef\]](#)
23. Houk, L.R.; Challa, S.R.; Grayson, B.; Fanson, P.; Datye, A.K. The definition of “critical radius” for a collection of nanoparticles undergoing Ostwald ripening. *Langmuir* **2009**, *25*, 11225–11227. [\[CrossRef\]](#)
24. Dagtepe, P.; Chikan, V. Quantized Ostwald ripening of colloidal nanoparticles. *J. Phys. Chem. C.* **2010**, *114*, 16263–16269. [\[CrossRef\]](#)
25. Xiao, X.; Zheng, C.X.; Lu, M.L.; Zhang, L.; Liu, F.; Zuo, X.X.; Nan, J.M. Deficient Bi₂₄O₃₁Br₁₀ as a highly efficient photocatalyst for selective oxidation of benzyl alcohol into benzaldehyde under blue LED irradiation. *Appl. Catal. B-Environ.* **2018**, *228*, 142–151. [\[CrossRef\]](#)

26. Shi, J.L.; Feng, K.; Hao, H.; Ku, C.; Sit, P.H.-L.; Teoh, W.Y.; Lang, X. 2D sp² Carbon-conjugated covalent organic framework with pyrene-tethered TEMPO intercalation for photocatalytic aerobic oxidation of sulfides into sulfoxides. *Sol. RRL* **2022**, *6*, 210060.
27. Xing, W.; Liu, C.; Zhong, H.; Zhang, Y.; Zhang, T.; Cheng, C.; Han, J.; Wu, G.; Chen, G. Phosphate group-mediated carriers transfer and energy band over carbon nitride for efficient photocatalytic H₂ production and removal of rhodamine B. *J. Alloy Compd.* **2022**, *895*, 162772. [[CrossRef](#)]
28. Zhang, L.; Wang, W.Z.; Sun, S.M.; Jiang, D.; Gao, E.P. Selective transport of electron and hole among {001} and {110} facets of BiOCl for pure water splitting. *Appl. Catal. B-Environ.* **2015**, *162*, 470–474. [[CrossRef](#)]
29. Wang, L.; Zhao, X.; Lv, D.D.; Liu, C.W.; Lai, W.H.; Sun, C.Y.; Su, Z.M.; Xu, X.; Hao, W.C.; Dou, S.X.; et al. Promoted photocharge separation in 2D lateral epitaxial heterostructure for visible-light-driven CO₂ photoreduction. *Adv. Mater.* **2020**, *32*, 2004311. [[CrossRef](#)]
30. Wang, M.; Tan, G.Q.; Zhang, D.; Li, B.; Lv, L.; Wang, Y.; Ren, H.J.; Zhang, X.L.; Xia, A.; Liu, Y. Defect-mediated Z-scheme BiO_{2-x}/Bi₂O_{2.75} photocatalyst for full spectrum solar-driven organic dyes degradation. *Appl. Catal. B-Environ.* **2019**, *254*, 98–112. [[CrossRef](#)]
31. Chen, X.; Zhang, X.; Li, Y.H.; Qi, M.Y.; Li, J.Y.; Tang, Z.R.; Zhou, Z.; Xu, Y.J. Transition metal doping BiOBr nanosheets with oxygen vacancy and exposed {102} facets for visible light nitrogen fixation. *Appl. Catal. B-Environ.* **2021**, *281*, 119516. [[CrossRef](#)]
32. Bai, Y.; Ye, L.; Chen, T.; Wang, L.; Shi, X.; Zhang, X.; Chen, D. Facet-dependent photocatalytic N₂ fixation of bismuth-rich Bi₅O₇I nanosheets. *ACS Appl. Mater. Interfaces* **2016**, *8*, 27661–27668. [[CrossRef](#)]
33. Chen, Y.; Wang, F.; Cao, Y.H.; Zhang, F.Y.; Zou, Y.Z.; Huang, Z.A.; Ye, L.Q.; Zhou, Y. Interfacial oxygen vacancy engineered two-dimensional g-C₃N₄/BiOCl heterostructures with boosted photocatalytic conversion of CO₂. *ACS Appl. Energ. Mater.* **2020**, *3*, 4610–4618. [[CrossRef](#)]